CHEMISTRY OF MATERIALS

pubs.acs.org/cm

Article

High-Pressure Electronic and Vibrational Properties of $NiMoO_4$ in the α and ω Phases: Experimental and Density Functional Theory Study

Luis Gómez, Alfonso Muñoz, Helmut Ehrenberg, and Fernando Rodriguez*

Cite This: https://doi.org/10.1021/acs.chemmater.6c00849

Read Online

ACCESS | Metrics & More | Article Recommendations | Supporting Information

ABSTRACT: This work investigates the electronic and vibrational properties of $NiMoO_4$ single crystals by optical absorption and Raman spectroscopy under high pressure (0−20 GPa). We focus on the α-$NiMoO_4$ phase and the metastable ω-$NiMoO_4$ phase, which forms under compression above 14.5 GPa, thereby enriching the polymorphism of this material. Experimental Raman frequencies and their pressure dependence show excellent agreement with density functional theory (DFT) calculations, enabling precise mode assignment for the monoclinic $C2/c$ (α-phase) and $P2/c$ (ω-phase) structures. We provide consistent links between structure, vibrations, and electronics for α- and ω-$NiMoO_4$—essential for applications relying on nanoscale materials where phase mixtures (mostly α and β phases) are common. Optical absorption spectra reveal five weak subgap bands associated with Ni^{2+} d-d transitions, together with an absorption edge corresponding to an indirect band gap of 2.99 eV for the α-phase and a direct band gap of 1.7 eV for the metastable ω-phase at ambient conditions—thus clarifying the semiconducting nature of the ω-phase, contrary to prior claims of metallicity. Using pressure-tuned Tanabe−Sugano analysis, we unambiguously assign these subgap features. Notably, some previously undetected Ni^{2+} bands become visible under compression, as pressure enables adequate tuning of excited states to reach Fano resonance conditions. In addition, we provide a detailed experimental characterization of the pressure-induced $\alpha \rightarrow \omega$ transition. Remarkably, the high-pressure ω phase is quenchable to ambient conditions, where it remains metastable. We explain the large pressure hysteresis ($\alpha \rightarrow \omega$ at ∼15 GPa vs DFT-predicted stability above ∼1 GPa) by its high activation energy and a volume change of 13%. The ω phase exhibits enhanced absorption characteristics—with a direct band gap of 1.7 eV—making it highly attractive for photoactive applications. Our combined experimental and DFT results provide a consistent interpretation of the pressure-driven evolution of structure, vibrations, and electronic properties in this material system.

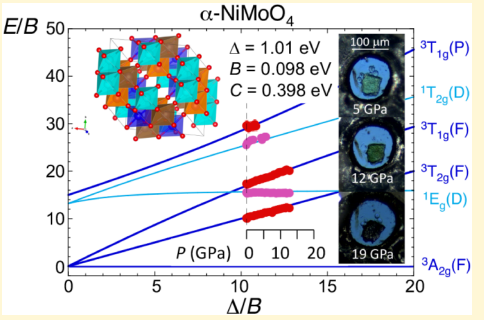

INTRODUCTION

$NiMoO_4$ has attracted significant interest due to its favorable properties for various applications, including energy storage,[1] high-performance anodes in Li-batteries,[2] supercapacitors[3−5] photocatalysis[6,7] and water splitting.[7] However, studies of its optical and vibrational properties remain limited and often focus on nanostructured forms, which typically consist of mixtures of α and β phases (Figure 1). Nanostructures introduce complications such as surface effects and quantum confinement, making structural characterization challenging. To address this, we present a combined experimental and theoretical investigation of the optical and vibrational properties of α-$NiMoO_4$ single crystals. Using single crystals eliminates effects related to nanostructuring, providing a fundamental understanding of the intrinsic properties of this material. Furthermore, we explore how these properties evolve with pressure, offering insights into how lattice compression and structural transitions influence material behavior.

This study pursues four main goals: (1) Structural correlations across polymorphs. We provide a consistent link between structure, vibrations, and electronics for α- and ω-$NiMoO_4$. This knowledge is essential for applications relying on nanoscale materials where phase mixtures (mostly α and β phases) are common. (2) Subgap Ni^{2+} bands. We unambiguously assign weak subgap features (often misattributed to impurities or excitons) using pressure-tuned Tanabe−Sugano analysis. (3) Pressure-tuned Fano resonance. We apply external pressure to detect previously unobserved Ni^{2+} bands by tuning excited states to achieve or decouple Fano resonance conditions. (4) ω-phase metastability. We investigate whether this ω-phase can be accessed from α-$NiMoO_4$ by applying pressure at ambient conditions, and whether this phase can be retained metastably upon decompression. By combining

Received: March 23, 2026
Revised: July 9, 2026
Accepted: July 10, 2026

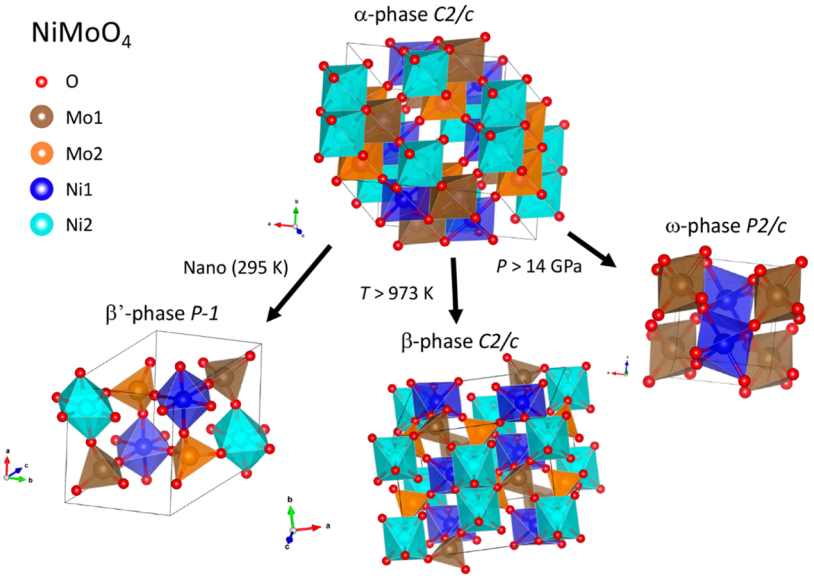

Figure 1. Crystal structures of $NiMoO_4$. The central structure corresponds to the α-$NiMoO_4$ phase (monoclinic $C2/c$) at ambient pressure and room temperature. The other two phases are the β-$NiMoO_4$ phase (monoclinic $C2/c$) above 973 K and ambient pressure[8,9] and the ω-$NiMoO_4$ phase (monoclinic $P2/c$)—the high-pressure phase II[10]—above 14 GPa at room temperature. Note that both α and β phases have two distinct Ni^{2+} sites (1 and 2) making the Ni−O−Ni superexchange pathways weaker than in the ω-phase, which has equivalent Ni sites along chain-like edge-sharing NiO_6 octahedra. Molybdenum coordination corresponds to tetrahedra, distorted octahedra, and regular octahedra in β, α, and ω phases, respectively. It must be noted that β[11] or β'phases (Figures S3 and S4 in the Supporting Information) can be stabilized at room temperature in $NiMoO_4$ nanoparticles; their lattice and structural parameters are given in Table 1.

Table 1. Experimental and DFT-Calculated Crystallographic Data for α, β, and ω Phases of $NiMoO_4$

Single crystals (bulk)								
Phase	Space group	a (Å)	b (Å)	c (Å)	β (°)	V (Å^3/Ni)	T (K)	Refs
α	$C2/c$	9.566(1)	8.734(1)	7.649(1)	114.22(1)	72.85(3)	298	8,9,12
α	$C2/c$	9.636(2)	8.835(1)	7.617(1)	113.82(2)	74.15(3)	947	8 and 9
β	$C2/c$	10.1588(5)	9.2135(4)	7.0034(3)	107.099(2)	78.317(5)	973	8 and 9
β	$C2/c$	10.13(2)	9.28(2)	7.02(2)	107.2(1)	78.75(3)	1148	31
β	$C2/c$	10.177(1)	9.243(1)	7.011(1)	107.09(2)	78.80(3)	1201	8 and 9
ω	$P2/c$	4.6559(2)	5.6808(2)	4.9112(1)	89.51(2)	64.95(1)	298	10
Nanoparticles								
α	$C2/c$	9.59(1)	8.75(2)	7.64(2)	114.1(1)	73.2(3)	RT	5
α	$C2/c$	9.597(1)	8.767(1)	7.667(1)	114.18(1)	73.56(1)	RT	38
β	$C2/c$	10.1(1)	9.12(1)	6.99(1)	106	77.6(3)	RT	11
DFT calculations								
α	$C2/c$	9.369	8.413	7.010	113	73.6	0	34
β	$C2/c$	—	—	—	—	80.6	0	34
ω	$P2/c$	—	—	—	—	63.0	0	34
ω	$P2/c$	4.6226	5.6866	4.9308	89.98	64.8	0	43
ω		4.5952	5.6774	4.8686	90.83	63.5	0	This work
α	$C2/c$	9.5837	8.7557	7.6704	114.17	73.4	0	This work
β'	Triclinic $P-1$	6.8297	6.8311	7.0165	α = 77.086 β = 77.074 γ = 84.095	77.63	0	This work (Figures S3, S4)

different experimental techniques, we provide a comprehensive characterization of the $\alpha \rightarrow \omega$ phase transition. We rationalize the pronounce pressure hysteresis—observed at ∼15 GPa for the forward transition, compared to DFT-predicted stability onset at ∼1 GPa—and demonstrate that, contrary to earlier claims of metallicity, ω-$NiMoO_4$ is a direct wide-gap semiconductor (1.7 eV), whereas α-$NiMoO_4$ is an indirect wide-gap semiconductor (2.99 eV).

In this work, we investigate the vibrational and optical properties of α-$NiMoO_4$ single crystals under pressure, including across the pressure-induced transition to the high-pressure phase. Our study is supported by DFT calculations of phase stability, phonon frequencies, and their pressure dependence, electronic dispersion curves, density of states (DOS), and gap energy as a function of pressure.

EXPERIMENTAL SECTION

Synthesis and Structure

Single-crystal platelets of α-$NiMoO_4$ were synthesized as described previously.[12] Their monoclinic structure (space group $C2/c$) was

https://doi.org/10.1021/acs.chemmater.6c00849
Chem. Mater. XXXX, XXX, XXX−XXX

confirmed by X-ray diffraction, yielding the lattice parameters listed in Table 1. Crystal orientation was verified by X-ray diffraction, Raman spectroscopy, and polarizing microscopy. Single-crystal X-ray diffraction data were collected at 298 K using a Rigaku SuperNova four-circle diffractometer equipped with a microfocus sealed X-ray tube (SuperNova Mo X-ray Source, λ = 0.71073 Å, mirror monochromator) and a HyPix Hybrid Pixel Array Detector. A total of 2877 reflections were measured in the θ range of 2.9124° to 29.8368° (index ranges: $-10 \le h \le 8$, $-10 \le k \le 12$, $-9 \le l \le 13$), yielding a data set with an R_{int} of 0.0368 and a $\sigma(I)/I$ of 0.0511. Crystallographic planes were identified for several single-crystal habits exhibiting (110) as preferred cleavage planes (Figure S1 in the Supporting Information).

Polarized optical microscopy and Raman spectroscopy (Figure S1) were systematically used to check the crystal quality and uniformity. Observations under crossed polarizers allowed us to select single-domain platelets in high-pressure measurements. Raman mapping revealed <1 cm^{-1} variation in peak positions and <5% variation in relative intensities across the crystal.

High-Pressure Measurements

Two diamond anvil cells (DACs) were used: a Boehler–Almax DAC with 350 μm anvil culets and a 150 μm sample chamber, and a membrane DAC with 450 μm anvil culets and a 150 μm chamber. The pressure cavity was machined from a 200 μm-thick Inconel 625 gasket, preindented to 40 μm. The sample was loaded alongside microrubies (~10 μm) for pressure calibration,[13] with spectroscopic paraffin oil as the pressure-transmitting medium. This provides a quasi-hydrostatic pressure in the chamber of ~5% in the 0–20 GPa range.[14,15] The membrane DAC allowed precise pressure control during both compression and decompression cycles. The Boehler-Almax DAC was equipped with high-transmission diamonds for optical absorption studies.

Optical Extinction, Reflectance, and Raman Spectroscopy

Raman spectra were acquired using a Horiba T64000 spectrometer with 514.5 nm excitation from a Coherent Innova 70C Ar^+/Kr^+ laser. Measurements were performed in backscattering geometry on α-$NiMoO_4$ platelets oriented perpendicular to the monoclinic <1−10> direction in the (1−10) plane (Figure S1), with a spectral resolution of 1.2 cm^{-1}.

High-pressure measurements were conducted using a microscope adapted for microspectroscopy, equipped with reflective objectives to focus light onto the sample inside the DAC. Transmitted light was collected with another reflective objective and directed via optical fiber to a spectrometer.[16] Reflectance spectra were obtained with the same microscope by adapting an optical fiber bundle containing seven fibers: six for excitation with a tungsten lamp and one central fiber to detect the reflected/scattered light. The opposite fiber configuration was used working with DACs. The reflectance spectra (I/I_0) in the DAC were acquired using the excitation configuration shown in Figure S1d. The reflected light was detected through the six fibers around the excitation fiber.

Computer Simulations

First-principles simulations were performed using Density Functional Theory, DFT,[17] with the Vienna ab initio Simulation Package, VASP.[18,19] The projector augmented-wave, PAW, pseudopotentials[20,21] were employed and the plane-wave kinetic cutoff was extended up to 540 eV to ensure highly accurate converged results. The integrations over the Brillouin zone, BZ, were carried out with k-special points sampling of 6 × 6 × 4. The exchange-correlation energy was described by means of the generalized gradient approximation, GGA, with the Perdew–Burke–Ernzerhof functional for solids (PBEsol).[22] To treat strongly correlated states properly, the DFT +U method of Dudarev et al.[23] was employed with an effective U_{eff} = U − J = 6.2 eV for the Ni atoms.[24] The antiferromagnetic configuration was found to be the lower in energy. Atomic positions and the unit cell parameters were fully optimized at selected volumes, with force convergence ≤0.003 eV/Å and stress tensor deviations from hydrostatic form ≤0.1 GPa. The resulting volumes, energies, and pressures were fitted to a Birch–Murnaghan equation of state[25] to obtain the theoretical equilibrium volume, bulk modulus, and pressure derivatives. Lattice-dynamic calculations of the phonon modes at the zone center (Γ-point) were carried out using direct force-constant approach with the Phonopy package.[26] These calculations provide normal-mode frequencies, symmetries, and polarization vectors, allowing identification of irreducible representations and phonon mode characters at the Γ-point. A 2 × 2 × 2 supercell was used to obtain phonon dispersion and check dynamical stability. Electronic band structure calculations were performed combining VASP and the VASPKIT package.[27] Although semilocal functionals are known to generally underestimate band gaps[28−30] in the present case the PBEsol-based DFT band gaps for both the α and ω phases will be compared with the measured values for self-consistency.

RESULTS AND DISCUSSION

Polymorphism of $NiMoO_4$

$NiMoO_4$ crystallizes in at least three monoclinic phases,[31] two of which—α and β (space group $C2/c$)—are stable at ambient pressure.[12,31,32] A denser third phase, denoted ω,[10,33,34] also referred to as phase II or high-pressure phase,[10,31,35] is synthesized under high pressure and adopts a monoclinic $P2/c$ structure[31] (Figure 1). Lattice parameters for these phases are summarized in Table 1 based on prior crystallographic studies of bulk crystals.[10,12,31,35] In nanoparticles, all three phases can be stabilized at ambient conditions, either as pure phases or mixtures.[2,11,36−39]

The crystal structure of $NiMoO_4$ consists of chains of edge-sharing NiO_6 octahedra, along with a network of either MoO_4 tetrahedra or MoO_6 octahedra depending on the phase, which correlates with lattice volume: tetrahedral coordination in β-$NiMoO_4$, distorted octahedral coordination in α-$NiMoO_4$, and more regular octahedral coordination in ω-$NiMoO_4$ (Figure 1). The α and β phases have similar enthalpies, enabling their stabilization at ambient conditions. The α phase transforms to β above 973 K and reverts to α below 520 K.[8,9,36] In the slightly less-dense β-phase, Mo^{6+} ions are tetrahedrally coordinated, forming an independent $[MoO_4]^{2-}$ framework. The α phase can be viewed as a compressed β phase in which two oxygen ligands of one MoO_4 unit are shared with a neighboring MoO_4, resulting in a distorted octahedral (4 + 2) coordination with off-center Mo^{6+} ions. This compression creates two distinct octahedral sites for Ni^{2+} (sites 1 and 2), alternating along the edge-sharing chains parallel to the b-axis. The high-pressure ω phase is denser and adopts a wolframite-type structure in which both Ni^{2+} and Mo^{6+} exhibit nearly regular octahedral coordination.

The connectivity of $[NiO_6]$ octahedral chains strongly influences the Ni–O–O–Ni superexchange interactions, leading to variations in antiferromagnetic order.[10,12,40,41] α-$NiMoO_4$ (described as a rock-salt structure[35]) is antiferromagnetic with a Curie–Weiss temperature Θ_{CW} = 22 K and a Néel temperature T_N = 19 K[40,41] whereas ω-$NiMoO_4$ is antiferromagnetic with Θ_{CW} = −100 to −120 K and T_N = 60 K.[10,42] To our knowledge, no magnetic data have been reported for the β phase.

Notably, both α- and β-$NiMoO_4$ structures—stable in single crystals at ambient conditions and above 973 K, respectively (Figure S2)[8,9,31]—have also been stabilized at the nanoscale under ambient conditions.[7,37] Table 1 includes lattice parameters of α-, β- (or β'-), and ω-$NiMoO_4$ nanoparticles from the literature.[5,11,38,39] These data suggest that nanoparticles of α and β (or β') phases are approximately 1% less dense than their bulk counterparts, in contrast to metallic

https://doi.org/10.1021/acs.chemmater.6c00849
Chem. Mater. XXXX, XXX, XXX−XXX

nanoparticles, which are typically denser at the nanoscale.[44] Although the structure of β-$NiMoO_4$ nanoparticles has been characterized by XRD,[11] a direct comparison with bulk crystal data[31] is complicated because nanoparticle measurements were conducted at room temperature whereas bulk data were obtained at elevated temperatures (1148 K[31] and 973 K),[8,9] given that the β phase reverts to α at room temperature. Moreover, reported structural data for $NiMoO_4$ nanoparticles vary across studies (Table 1). Typically, α- and β-$NiMoO_4$ nanoparticles are identified by comparing XRD patterns with reference files: α-$NiMoO_4$ with JCPD: 33−0948[7] and ICSD: 98−008−1059;[5] β-$NiMoO_4$ with JCPD: 12−0348[4] and 45−142.[7] While this approach is suitable for α-$NiMoO_4$, it is less reliable for β-$NiMoO_4$ because the reference patterns correspond to high-temperature data obtained at 1148 K,[31] leading to significant Bragg peak shifts relative to room temperature values. Detailed powder XRD analysis of β-$NiMoO_4$ nanoparticles at room temperature has been reported,[11] with lattice parameters listed in Table 1. These cannot be directly compared to β-$NiMoO_4$ bulk data at the same temperature due to β-phase instability. However, temperature-dependent XRD measurements on bulk crystalline $NiMoO_4$ powder (Figure S2)[8,9] allow extrapolation of β-phase lattice parameters to room temperature using the thermal expansion coefficient. From Table 1 and Figure S2, we derive a thermal coefficient $\alpha = \frac{1}{V}\left(\frac{\partial V}{\partial T}\right)_{P=0} = 2.7 \times 10^{-5}\ K^{-1}$ between 973 and 1201 K.[8,9] Assuming linear volume dependence $V(T)$, the estimated lattice volume of β-$NiMoO_4$ bulk at 298 K is V = 76.9 Å^3/Ni, close to the measured value (77.6 Å^3/Ni) in β-$NiMoO_4$ nanoparticles. The volume increase from α (73.56 Å^3/Ni) to β (77.6 Å^3/Ni) phases in nanoparticles is 5.4%, consistent with the 5.5% increase observed at the $\alpha \rightarrow \beta$ transition at 973 K (Figure S2 in the Supporting Information).[8,9] These results validate the structural data reported for β-$NiMoO_4$ nanoparticles at 298 K (Table 1).

Although the monoclinic structure is widely assumed for β-$NiMoO_4$ nanoparticles based on XRD data,[34] our DFT-calculations show that the triclinic (space group $P-1$) is more stable than the monoclinic ($C2/c$) structure (Table 1). Furthermore, the XRD pattern obtained for $NiMoO_4$ nanoparticles with major β-phase is better described by the DFT-calculated triclinic structure (Figures S3 and S4 in the Supporting Information). This result may explain why the β phase—which cannot be stabilized in $NiMoO_4$ bulk at ambient conditions since it transforms back to α-$NiMoO_4$—has been observed in nanostructures. The nanoscale likely provides an adequate structural environment to stabilize the β' (or β) phase relative to the α phase.

The distinct structural and magnetic characteristics of α-$NiMoO_4$ significantly influence its optical properties compared to ω-$NiMoO_4$ and its wolframite-type analogue $NiWO_4$.[43,45]

Vibrational Properties

Figure 2 presents the room-temperature Raman spectrum of an α-$NiMoO_4$ single-crystal (110) platelet (80 × 30 × 11.3 μm^3). The monoclinic ($C2/c$) structure of α-$NiMoO_4$ gives rise to 72 vibrational modes: three acoustic (A_u + 2 B_u) and 69 optical (14 A_u + 19 B_u + 19 A_g + 17 B_g). Of the 36 Raman-active modes (A_g and B_g symmetries), we observe 24 peaks in the ambient-pressure spectrum; the remaining 12 peaks have low intensity or are unresolved due to overlap. Their pressure evolution is shown in Figure 3. Although most peaks shift to higher frequencies with pressure, the spectrum remains stable up to 14.5 GPa, beyond which significant changes occur, indicative of a transition to the high-pressure ω-$NiMoO_4$ phase. This high-pressure wolframite-type phase is metastable upon pressure release at ambient conditions.

Raman spectroscopy, alongside XRD, is commonly used to characterize $NiMoO_4$ nanoparticles, particularly to distinguish between α, β, and ω phases and assess their relative abundances. This is especially relevant for nanoparticles

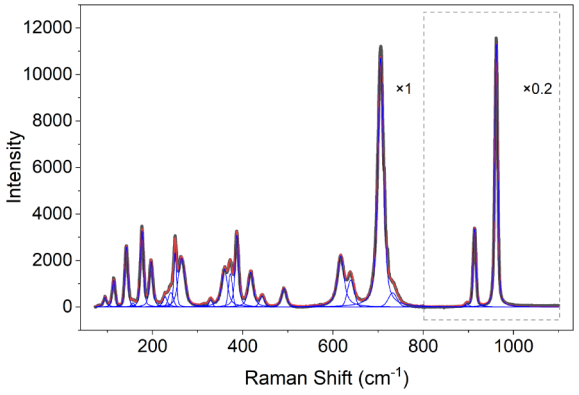

Figure 2. Raman spectrum of α-$NiMoO_4$ at ambient conditions obtained in back scattering configuration in a (110) single-crystal platelet. The observed 24 peaks have been described by fitting the measured spectrum (black color) to the sum of 24 Lorentzian functions (red color) providing the vibrational frequency with an accuracy of 1 cm^{-1}, and typical full width at half-maximum (fwhm) of ∼5−10 cm^{-1} (blue color). The spectrum is divided in three regions according to the peak intensities. The peaks were assigned to vibrational modes of either A_g or B_g symmetry of the monoclinic $C2/c$ structure by comparing the measured and DFT-calculated vibrational frequencies and the corresponding pressure shifts. These results and peak assignment are collected in Table S1.

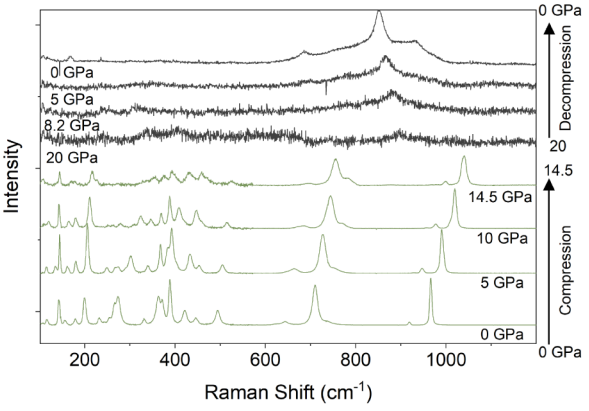

Figure 3. Room-temperature pressure dependence of the Raman spectrum of $NiMoO_4$. The peaks in the α-phase (green color) shift all to higher frequencies and remain stable up to 14.5 GPa. Beyond this pressure the spectrum (gray color) abruptly changes leading to a structureless polycrystalline spectrum with broader peaks at 20 GPa. This high-pressure spectrum remains upon pressure release thus showing metastability of the ω-$NiMoO_4$ phase at ambient conditions. The ambient-pressure spectrum of ω phase shows a narrower-peak structure compared to the spectrum at 20 GPa, although peaks are still broad due internal stress likely due to multigrain formation across the α to ω first-order phase transition. The measured and DFT-calculated vibrational frequencies and their corresponding pressure shifts are collected in Tables S1 and S2, and represented in Figure 4.

https://doi.org/10.1021/acs.chemmater.6c00849
Chem. Mater. XXXX, XXX, XXX−XXX

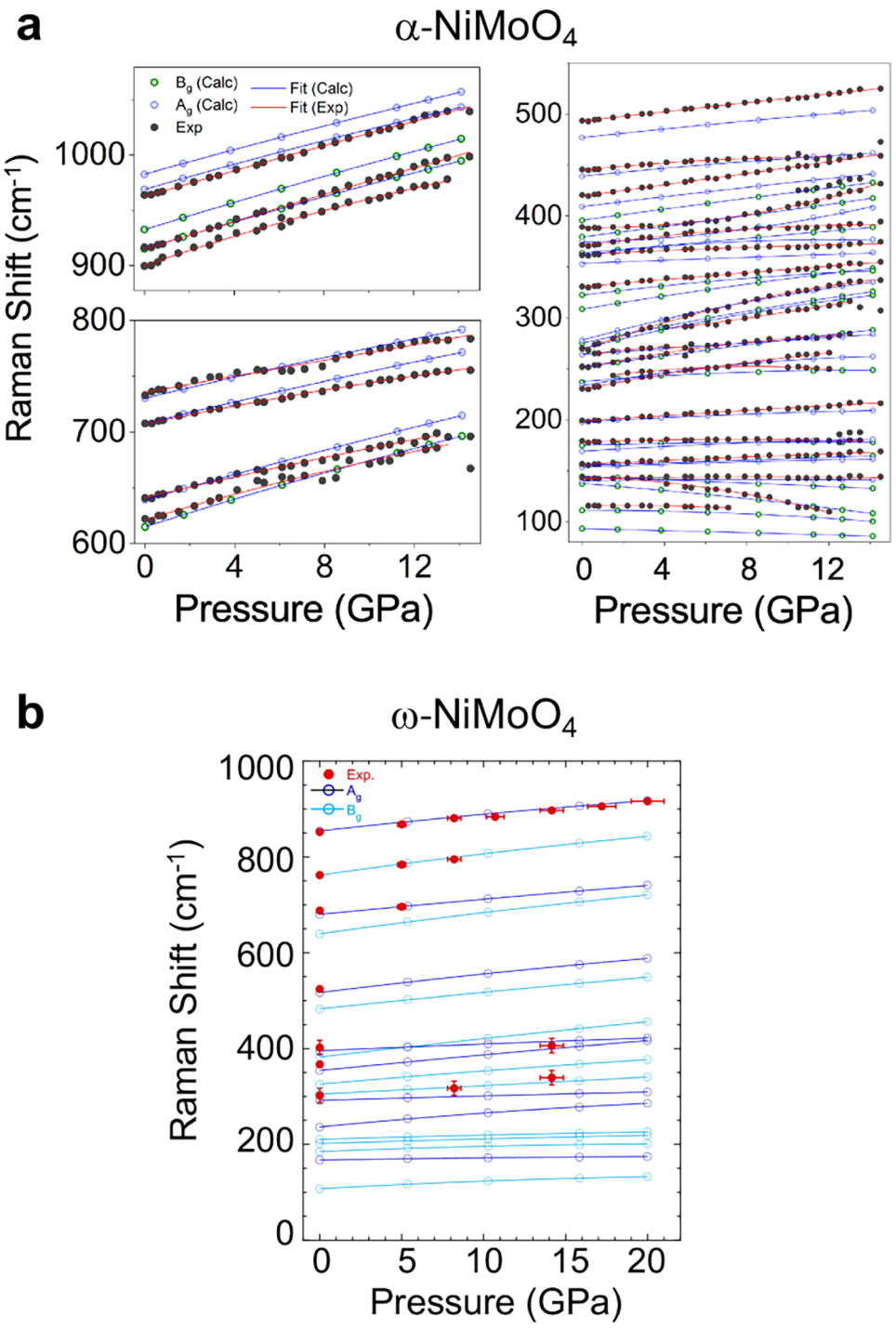

Figure 4. Variation of the Raman frequencies corresponding to vibrational modes at Γ-point of α-$NiMoO_4$ (a) and ω-$NiMoO_4$ (b) with pressure at room temperature. Black circles and red lines in (a) correspond to experimental frequencies, $\nu^i(P)$ and their fits to a second-order polynomial as $\nu^i(P) = \nu_0^i(P) + aP + bP^2$, respectively. Blue open circles and lines in (a) and (b) correspond to DFT-calculated frequencies and their least-squares fittings to $\nu_{DFT}^i(P) = \nu_{DFT_0}^i(P) + cP + dP^2$. Peak assignment was achieved by comparing the measured and DFT-calculated frequencies and their pressure shift coefficients for each mode are collected in Tables S1 and S2. The scarce number of experimental points in (b) is due to the stressed multigrain Raman spectra in ω-$NiMoO_4$ after transition from α-$NiMoO_4$ at 14.5 GPa. Because of its metastability, the Raman spectrum was obtained in decompression from 20 GPa to ambient pressure. Errors are indicated by bars or the symbol size.

synthesized for applications requiring specific phase compositions.[1,4,5,11,36,37,39,46,47] High-frequency modes associated with Mo−O stretching vibrations—a detailed description of atomic displacements of the highest frequency mode is given in Figure S7, and Tables S1−S3—appear at 707, 913, and 961 cm^{-1} in α-$NiMoO_4$, at 820, 890, and 935 cm^{-1} in β-$NiMoO_4$ within the 600−1100 cm^{-1} range,[1] and at 852 and 762 cm^{-1} in ω-$NiMoO_4$ providing a straightforward method for phase identification and quantification in nanoparticles.

The measured and calculated Raman frequencies at ambient pressure, along with the fitted parameters describing their pressure dependence using a second-order polynomial: $\nu(P)$ =

https://doi.org/10.1021/acs.chemmater.6c00849
Chem. Mater. XXXX, XXX, XXX−XXX

$\nu_0 + aP + bP^2$, are listed in Tables S1 and S2. The pressure dependence of the vibrational frequencies is shown in detail in Figure 4. Peak assignments in Tables S1 and S2 were made by comparing experimental data with DFT-calculated frequencies and pressure coefficients. These results serve as a reference for bulk α-$NiMoO_4$ single crystals. Notably, Raman data reported for α-$NiMoO_4$ nanoparticles or thin films[5,37,39,46,47] may exhibit slight shifts or broadening due to size effects and internal stresses, complicating accurate vibrational analysis. Tables S1 and S2 also include vibrational frequencies from the most comprehensive Raman spectrum reported for α-$NiMoO_4$ nanoparticles.[47]

Overall, phonon frequencies exhibit approximately linear pressure dependence with shift rates similar to theoretical predictions in the 0−14 GPa range, confirming the stability of α-$NiMoO_4$ within this interval. Above 14 GPa, Raman spectra broaden and lose structure, with major peaks shifting abruptly, consistent with a structural phase transition to the wolframite-type ω-$NiMoO_4$ phase. The phonon frequencies of the few experimental Raman peaks resolved above 14.5 GPa and during decompression from 20 GPa to ambient pressure in the metastable ω phase (Figure 3) are compared to DFT-calculated frequencies. The fair agreement between experiment and calculation supports our interpretation (Figure 4, and Tables S1 and S2).

Many molybdates undergo complex pressure-induced phase transitions; for example, $MgMoO_4$,[48] $CoMoO_4$,[49] $FeMoO_4$,[50] and $ZnMoO_4$[51] exhibit similar behavior. $MgMoO_4$ (isostructural to α-$NiMoO_4$ though referred to as β-$MgMoO_4$ at ambient pressure) transitions at lower pressure (~5 GPa), likely due to its larger volume (V_0/Mg = 80.14 Å^3[51,52] compared to α-$NiMoO_4$ (V_0/Ni = 72.85 Å^3.[31]

The proposed pressure-induced phase transition in $NiMoO_4$ is supported by earlier DFT predictions[34] and further corroborated by our DFT simulations for α and ω phases, schematically represented in Figure 1 and Figure S3. Our simulations indicate that the α and β phases converge within the $C2/c$ space group with similar enthalpies and lattice parameters, while the ω phase stabilizes in the denser monoclinic $P2/c$ structure, in agreement with experimental observations. The enthalpies of the α and β phases differ by only 10.3 meV per formula unit, while the ω phase is three times higher (34 meV). Although the α phase is slightly lower in enthalpy, these small differences account for the stability of these phases at ambient conditions.[8,10,12,38,39]

Theoretically, the $\alpha \rightarrow \omega$ transition pressure is estimated at ~1 GPa based on the crossing point of the enthalpy curves derived from calculated bulk moduli and their pressure derivatives (inset of Figure S3). In contrast, Raman spectroscopy places the transition at ~15 GPa (Figure 3), revealing significant hysteresis at room temperature.

Indeed, the volume change associated with the $\alpha \rightarrow \omega$ transition at ambient conditions is 13% (Table 1)[31,33] in agreement with DFT calculations at 0 K yielding a volume collapse of 13% (Table 1 and Figure S3). Beyond entropic contributions, these values indicate that the activation energy required to drive the phase transition demands either elevated temperatures or pressures substantially higher than the theoretical equilibrium value. This accounts for the pronounced hysteresis and the metastable retention of the ω phase upon pressure release (Figures 3 and 6). Consistent with this interpretation, ω-$NiMoO_4$ can be stabilized at ambient conditions through synthesis under high-pressure (P ~ 1−5 GPa) and high-temperature (T ~ 873−973 K) conditions.[10,31,33]

The $\alpha \rightarrow \omega$ transition is also foreshadowed by the evolution of the calculated phonon dispersion curves for α-$NiMoO_4$ at 0 and 14.1 GPa (Figure S5). Although experimental phonon dispersion data for α-$NiMoO_4$ are not available, we observe a softening of the acoustic Y-phonon branch at 14.1 GPa, indicative of incipient structural instability. In addition, the Raman spectrum of the metastable ω-$NiMoO_4$ (Figure 3), regardless its stressed multigrain structure, resembles the measured spectrum of ω-$NiMoO_4$ nanoparticles.[39] Their major peaks shift to lower frequencies compared to α-$NiMoO_4$ (852 and 762 cm^{-1} vs 961.7 and 913.6 cm^{-1}), in agreement with DFT-calculated frequencies (Figures 3 and 4, and Tables S1 and S2).

The overall consistency between Raman experiments and theoretical predictions provides strong support for an α-$NiMoO_4$ → ω-$NiMoO_4$ phase transition at ~15 GPa and room temperature.

Optical Properties

Figure 5 shows the optical extinction spectrum of an α-$NiMoO_4$ single crystal. The spectrum resembles reflectance or absorption spectra reported for α-$NiMoO_4$ nanoparticles.[37−39] Using single-crystal platelets allows direct measurement of the extinction (absorption + scattering) coefficient as a function of photon energy, facilitating accurate extraction of the band gap and Ni^{2+} d-d transitions, as well as analysis of band shapes and oscillator strengths.

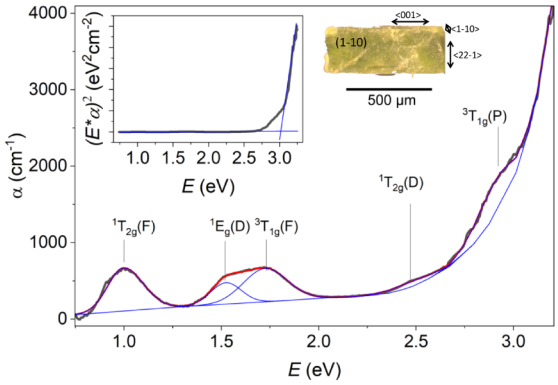

Figure 5. Optical extinction spectrum of a (1−10) single-crystal platelet of α-$NiMoO_4$ (680 × 260 × 120 μm^3) at ambient conditions. The absorption coefficient was obtained from the absorbance as $\alpha = 2.3 \times A/l$ with crystal thickness $l = 1.2 \times 10^{-2}$ cm. The measured spectrum (black) was fitted to the sum of five Gaussian functions (one for each subgap band) plus an absorption background (blue lines), with the sum represented in red. The band assignment corresponds to Ni^{2+} d^8 intraconfigurational crystal-field transitions based on their energies and pressure shifts (Figure 6, Table 2, and Table S4). The inset shows the absorption spectrum, $(\alpha \times E)^2$ vs E, to extract the direct band gap, E_g = 2.99 eV through Tauc's plots.[53] Measured and calculated transition energies (via Tanabe−Sugano semiempirical method[45,54,55] are collected in Table 2 and, Table S4 and shown in Figure S8.

The pressure evolution of the optical spectra is shown in Figure 6. Variations in the direct band gap and d-d transition energies are plotted in Figure 7, with fitting parameters summarized in Table 2. Pressure-dependent trends are crucial for assigning subgap features, such as Ni^{2+} intraconfigurational d-d transitions, following a methodology previously applied to

https://doi.org/10.1021/acs.chemmater.6c00849
Chem. Mater. XXXX, XXX, XXX−XXX

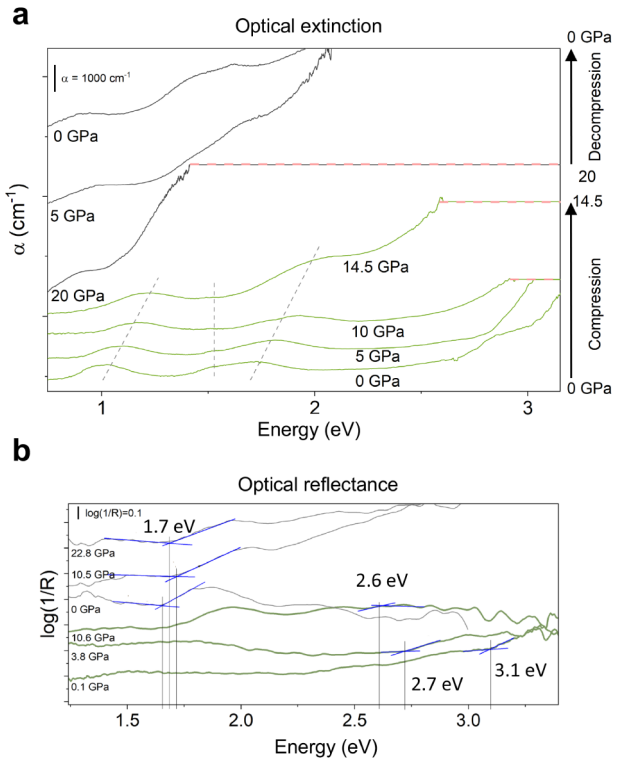

Figure 6. (a) Pressure dependence of the optical extinction spectrum of a (110) single-crystal platelet of $NiMoO_4$ in α (green) and ω (gray) phases at room temperature. The extinction coefficient was obtained from the absorbance as $\alpha = 2.3 \times A/l$ with a crystal thickness $l = 1.13 \times 10^{-3}$ cm and corrected for sample compression. Note the abrupt change experienced by the optical extinction spectrum across the $\alpha \rightarrow \omega$ transition at 14.5 GPa. (b) Reflectance spectra of the initial α phase and the recovered ω phase at different pressures, together with the DAC images showing the green-to-black piezochromism exhibited by this crystal in the 0−20 GPa range. Both the subgap bands and the band gap undergo an abrupt shift to lower energies: the direct gap shifts to ∼1.7 eV and the crystal-field splitting to ∼0.1 eV. The gap energy, band assignment, measured and calculated—via Tanabe−Sugano semiempirical method,[45,54,55] transition energies are collected in Table 2 and Figure 7, Table S4, and Figure S8.

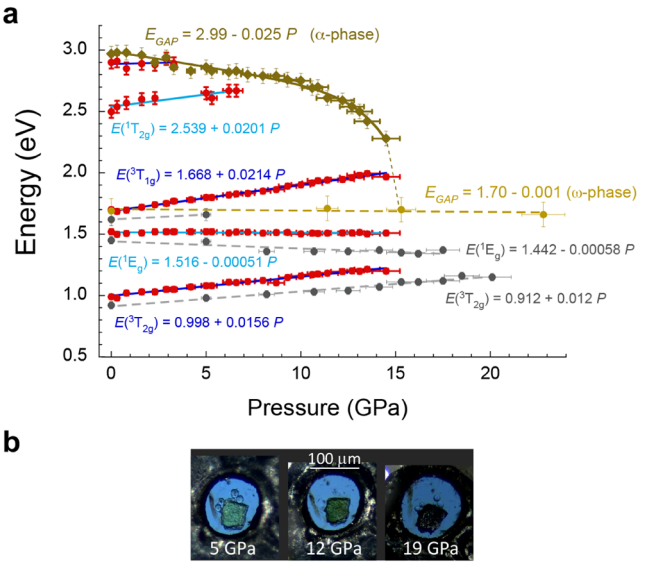

Figure 7. (a) Variation of the experimental transition energies of Ni^{2+} subgap bands and direct band gap with pressure at room temperature. Red and gray points represent experimental energies measured in compression and decompression, respectively. Blue solid and gray dashed straight lines correspond to least-squares linear fits of $E_i(P)$ (red and gray). The measured direct band gap obtained from Tauc plots[53] (reflectance spectra in the ω phase) E_{GAP} is shown in brown (light brown). Note its abrupt decrease δE_{GAP} = ∼0.3 eV across the $\alpha \rightarrow \omega$ transition at 14.5 GPa. Energy and pressure errors are indicated or contained within the symbol size. (b) DAC images showing the green-to-black piezochromism exhibited by the $NiMoO_4$ crystal in the 0−20 GPa range.

$NiWO_4$.[45] Both α-$NiMoO_4$ and $NiWO_4$ exhibit similar direct band gaps ($E_{GAP} \approx 3.0$ eV) and crystal-field splittings on Ni^{2+} ($\Delta = 10Dq \approx 1.0$ eV), despite the wolframite structure being ∼12% denser than α-$NiMoO_4$. While pressure reduces the band gap in both materials (typical for systems involving transition-metal ions with partially filled d orbitals[56]) the average Ni−O bond lengths are comparable (∼2.04 Å)[31,45] However, Mo^{6+} raises the top of the valence band compared to W^{6+}, reducing the gap in molybdates.[57] These competing effects—substitution of Mo^{6+} by W^{6+} and volume reduction from α-$NiMoO_4$ (∼73 Å^3/Ni) to $NiWO_4$ (∼64 Å^3/Ni)—result in comparable band gaps and crystal-field splittings.

The subgap bands are assigned to intraconfigurational d-d ($3d^8$) crystal-field transitions within the $(NiO_6)^{10-}$ complex (Figure 8). Specifically, they correspond to electronic transitions from the $^3A_{2g}(F)[t_{2g}^6e_g^2]$ ground state to the excited states $^3T_{2g}(F)$, $^3T_{1g,a}(F)[t_{2g}^5e_g^3]$, $^1E_g(D)[t_{2g}^6e_g^2]$, $^1T_{2g}(D)$, and $^3T_{1g,b}(P)[t_{2g}^5e_g^3]$, in order of increasing energy, in the low crystal-field limit ($\Delta/B < 10$). As the Tanabe−Sugano diagram shows in Figure 8, for $\Delta/B > 9.5$ (with $C/B = 4.1$), the $^3T_{1g,a}(F)$ energy exceeds that of $^1E_g(D)$. Transition energies as functions of Racah parameters B and C and the e_g−t_{2g} crystal-field splitting Δ[54] are provided in Table S4 and Figure S8. Measured and calculated (using the Tanabe−Sugano formalism[45,54,55]) transition energies and pressure shifts are listed in Table 2, with good agreement confirming the assignments.

Notable differences exist between the pressure-dependent behavior of Ni^{2+} subgap bands in α-$NiMoO_4$ and $NiWO_4$:[45] (1) Transition energies in α-$NiMoO_4$ are slightly higher, with pressure coefficients ∼50% larger. (2) In $NiWO_4$, the spin-allowed ($^3T_{1g,a}(F)$) and spin-forbidden ($^1E_g(D)$) electric-dipole transitions exhibit similar intensities across the entire pressure range. In contrast, in α-$NiMoO_4$ these intensities are comparable only at ambient conditions, where the bands have similar energies (1.52 and 1.72 eV, respectively). The $^1E_g(D)$ intensity decreases dramatically with pressure, becoming an order of magnitude weaker than $^3T_{1g,a}(F)$ above 4 GPa, with a corresponding decrease in the bandwidth (Figure 8b). This behavior is consistent with the loss of Fano resonance and allows unambiguous assignment of the subgap E_2 to $^1E_g(D)$: its intensity diminishes and its pressure shift is much smaller than that of $^3T_{1g,a}(F)$, in agreement with Tanabe−Sugano trends for d^8 ions (Tables 2 and S4, and Figure 8).

The oscillator strength for the first $^3T_{2g}(F)$ transition in α-$NiMoO_4$ is $f_{Ni} \sim 5 \times 10^{-5}$ (absorption coefficient $\alpha \sim 100$ cm^{-1}), typical of noncentrosymmetric Ni^{2+} sites (e.g., olivine[58]) and higher than in centrosymmetric Ni^{2+} sites such as $KMgF_3$:1%Ni^{2+} ($\alpha \sim 1$ cm^{-1}; $f_{Ni} \sim 5 \times 10^{-6}$, and $\sim 2 \times 10^{-7}$ for $^1E_g(D)$)[59] or MgO:0.03%Ni ($\alpha \sim 0.1$ cm^{-1}; $f_{Ni} \sim 10^{-6}$−10^{-7}).[60,61] Centrosymmetric sites with exchange-

https://doi.org/10.1021/acs.chemmater.6c00849
Chem. Mater. XXXX, XXX, XXX−XXX

Table 2. Transition Energies and Corresponding Pressure Shifts of the Five Sub-Gap Bands E_i (i = 1−5) of α-$NiMoO_4$ at Ambient Pressure[a]

Transition energy	E_1	E_2	E_3	E_4	E_5	E_g	σ
Band assignment[b] ($^3A_{2g}(F)\rightarrow$)	$^3T_{2g}(F)$	$^1E_g(D)$	$^3T_{1g}(F)$	$^1T_{2g}(D)$	$^3T_{1g}(P)$	$E_{g,dir}$	
Experimental E_i (P = 0; eV)	0.99	1.52	1.70	2.50	2.90	2.99	0.03 eV
Calculated E_i (Δ/B = 10.2; eV)	1.01	1.53	1.66	2.50	2.84	—	
Experimental $(\partial E_i/\partial P)_0$ (meV GPa^{-1})	15.6(5)	0.51(5)	21.4(5)	20.1(9)	—	25(2)	
TS calculated[c] $(\partial E_i/\partial P)_0$ (meV GPa^{-1})	15.6(5)	0.47(5)	18.7(5)	16.2(5)	28.1(5)	—	

[a]Band assignment corresponds to the excited state involved in the transition using O_h irreps. Superscripts correspond to the spin multiplicity, capital letters and subscripts are the corresponding irreps in octahedral crystal-field symmetry ($\Delta/B > 0$), and capital letters in parentheses represent the atomic angular momentum of the free ion in spherical symmetry ($\Delta/B = 0$). [b]The proposed band assignment to crystal-field transitions within the $3d^8$ configuration of Ni^{2+} is included. The comparison between experimental and calculated crystal-field derivatives of the transition energies are shown in last two rows. The crystal-field derivatives were calculated for Δ/B = 10.3 (eqs S1 and S2). The experimental and calculated energies at each pressure is given in Table S4. [c]Calculated pressure rate, $(\partial E_i/\partial P)_0$, from the Tanabe−Sugano diagram in the 10−13 range of Δ/B as $(\partial E_i/\partial P)_0 = (\partial E_i/\partial \Delta)_0 \times (\partial E_1/\partial P)_0$, where $E_1 = \Delta$, and i = 1−5.

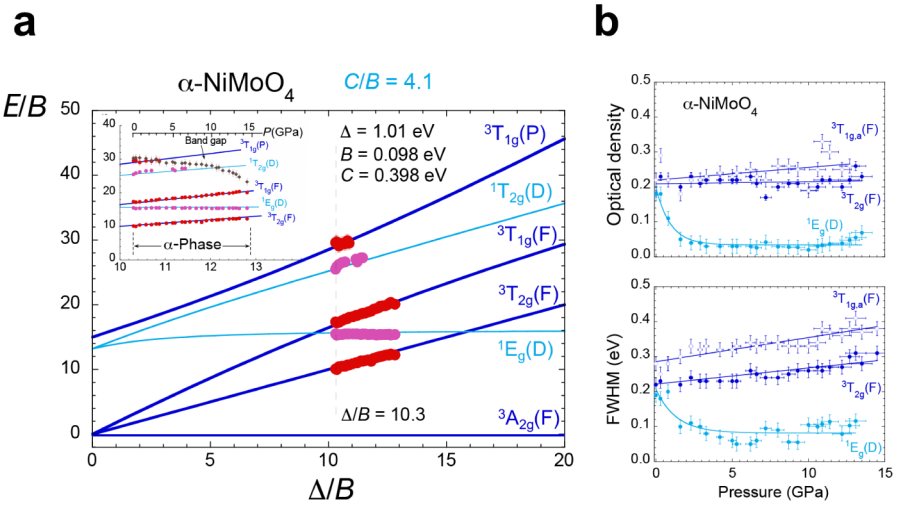

Figure 8. (a) Tanabe−Sugano diagram for $Ni^{2+}(3d^8)$ calculated with Racah parameters B = 0.098 eV and C = 0.398 eV over a Δ/B range of 0−20. Experimental transition energies of Ni^{2+} subgap bands and direct band gap for α-$NiMoO_4$ are included. Red and pink colors denote spin-allowed and spin-forbidden electric-dipole transitions, respectively. The inset magnifies the Δ/B range of 10−13, showing the direct band gap variation (brown) with error bars. (b) Pressure dependence of the measured optical density at band maximum and full-width at half-maximum (fwhm) of the Ni^{2+} spin-allowed $^3T_{2g}(F)$ (blue filled circles) and $^3T_{1g,a}(F)$ (blue open circles), and spin-forbidden $^1E_g(D)$ (magenta filled circles) transitions in α-$NiMoO_4$. Note the abrupt decrease in both optical density and fwhm of $^1E_g(D)$ in the 0−5 GPa range. This decrease is accompanied by a progressive decoupling (energy separation) of the $^3T_{2g}(F)$ and $^1E_g(D)$ bands. Pressure and energy error bars are indicated.

coupled ions often exhibit higher oscillator strengths due to the additional exchange mechanism[59,62] as in $KNiF_3$ ($\alpha \sim 100$ cm^{-1}; $f_{Ni} \sim 10^{-5}$ and 10^{-6} for $^3T_{2g}(F)$ and $^1E_g(D)$, respectively)[63] or NiO ($\alpha \sim 400$ cm^{-1}; $f_{Ni} \sim 5 \times 10^{-5}$).[64]

The transition mechanism is key to understanding some spectral features, particularly the proximity of the spin-forbidden $^3A_{2g}(F) \rightarrow {}^1E_g(D)$ and spin-allowed $^3A_{2g}(F) \rightarrow {}^3T_{1g,a}(F)$ transitions in oxides and fluorides.[45,59,62,63] Their distinct pressure shifts (Tables 2 and S4, and Figure 8) were critical for correct assignment in $NiWO_4$,[45] where both transitions show similar intensities despite different spin multiplicities, attributed to strong exchange interactions making both transitions spin-allowed in the coupled Ni−O−Ni system.[62] This behavior is not observed in α-$NiMoO_4$ (Figure 6) or $KNiF_3$.[63] In α-$NiMoO_4$ at ambient conditions, the two subgap bands at 1.52 and 1.72 eV overlap significantly, giving rise to coupling via Ni−O−Ni exchange or spin−orbit interaction within the $(NiO_6)^{10-}$ complex. We attribute the observed pressure-dependent behavior to a Fano resonance between the localized $^1E_g(D)$ state and the broad $^3T_{1g,a}(F)$ state, mediated by spin−orbit interaction.[65] This interaction mixes these excited states within a single $(NiO_6)^{10-}$ unit, producing a doublet with nearly equal intensities. Similar resonances have been observed for Cr^{3+} in fluorides and oxides[45,56] near the excited-state crossover (ESCO) point ($\Delta/B \sim 20$) for d^3 ions.[56] For $3d^8$ Ni^{2+}, the $^1E_g(D) \leftrightarrow {}^3T_{1g,a}(F)$ ESCO occurs at $\Delta/B \sim 10$. In most oxides[58] and specifically in $NiWO_4$[45] and α-$NiMoO_4$, Δ/B is 11.5 and 10.2, respectively (Figure 8), explaining the comparable band intensities. This trend is analogous but complementary to observations in $KNiF_3$ under pressure.[63] $KNiF_3$ has Δ/B = 7.7, placing the $^3T_{1g,a}(F)$ (1.550 eV) and $^1E_g(D)$ (1.916 eV) bands further from ESCO; the $^3T_{1g,a}(F)$ band is an order of magnitude more intense than the $^1E_g(D)$ band, with the latter at higher energy[63] (instead of lower energy as in oxides). Pressure blueshifts $^3T_{1g,a}(F)$ at 33 meV GPa^{-1}, bringing the bands into exact resonance at 11 GPa, where their intensities equalize due to Fano resonance.

This result strongly suggests that the transition mechanism in α-$NiMoO_4$ arises predominantly from odd-parity vibrations, noncentrosymmetric distortions in the $(NiO_6)^{10-}$ octahedra, and spin−orbit coupling—similar to Ni^{2+} impurity systems.

https://doi.org/10.1021/acs.chemmater.6c00849
Chem. Mater. XXXX, XXX, XXX−XXX

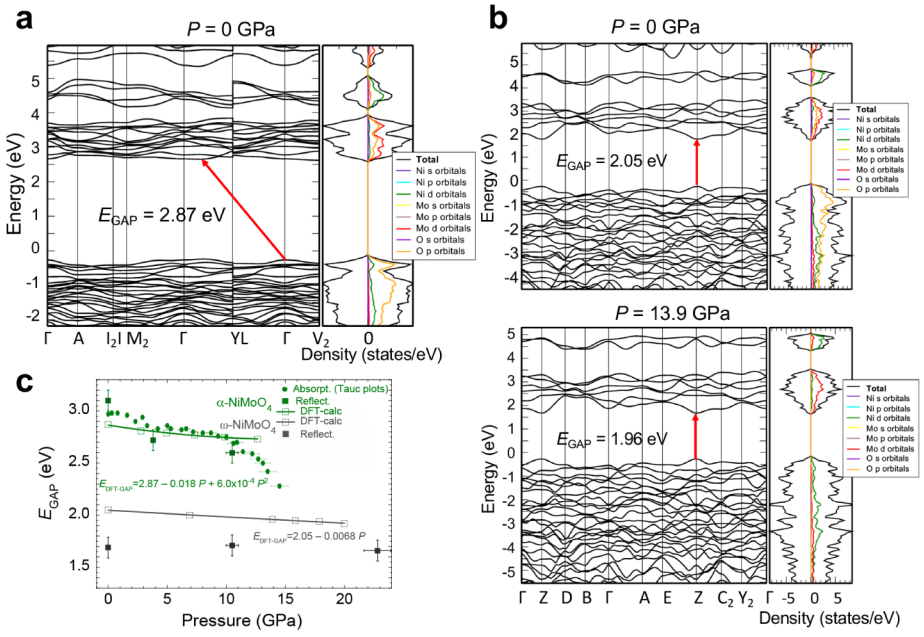

Figure 9. DFT-calculated electronic dispersion, density of states and gap energy of (a) α-$NiMoO_4$ (S.G. $C2/c$) at 0 K and 0 GPa, and (b) ω-$NiMoO_4$ (S.G. $P2/c$) at 0 K, 0 GPa (top) and 13.9 GPa (bottom). The valence band maximum (VBM) and conduction band minimum (CBM) do not change with pressure and are located at Γ(0 0 0) and Y(0.2105 0.2105 0), respectively, in α-$NiMoO_4$, and Z (0 0.5 0) (direct gap) in ω-$NiMoO_4$. (c) DFT-calculated pressure dependence of the gap energy for both α and ω phases. Note that the ω-phase gap is ∼1 eV lower than in α. Lines correspond to least-square fit to the calculated gap energies E_{GAP}.

The weaker exchange-mediated activation of $^1E_g(D)$ in α-$NiMoO_4$ compared to $NiWO_4$ likely stems from differences in superexchange pathways. In $NiWO_4$, superexchange involves equivalent Ni^{2+} sites (T_N = 60 K)[42] whereas in α-$NiMoO_4$ it involves two distinct Ni^{2+} sites (1 and 2), resulting in weaker interactions as reflected by its lower Néel temperature (T_N = 18 K).[40,41] Consequently, spin-dependent transition mechanisms activated by exchange are less effective in α-$NiMoO_4$, consistent with our spectroscopic observations.

Band Gap and ω-Phase Properties. The direct band gap of α-$NiMoO_4$ is 2.99 eV at ambient pressure, decreasing initially at −25 meV GPa^{-1} (Figures 6 and 7). This pressure-induced reduction causes higher-energy Ni^{2+} subgap states to merge with the band-edge tail, complicating their analysis (Figure 6). Such band gap narrowing under compression is typical in molybdates and wolframites featuring partially filled d-orbitals, where Ni^{2+} states contribute to raising the valence band maximum.[66] DFT simulations confirm this trend and provide direct band gap energies close to the measured values (Figures 7 and 9). It must be noted that while semilocal functionals are known to generally underestimate band gaps[28−30] in the present case the PBEsol-based DFT band gaps for both the α and ω phases are actually comparable to, or slightly larger than, the experimental measured values. This agreement provides self-consistent support for our interpretation of the pressure-induced evolution and confirms the semiconducting character of the ω phase. Above ∼12 GPa, the measured gap decreases quadratically, reaching 2.28 eV at 14.5 GPa—just before the phase transition to ω-$NiMoO_4$—which then sharply reduces the direct band gap to 1.7 eV at 15 GPa. The ω phase is quenchable to ambient pressure, remaining stable upon decompression, as confirmed by Raman and absorption spectroscopy (Figures 3 and 6). Broadening of optical and Raman bands—likely due to multigrain formation or microcracking during the transition—limits detailed spectroscopic analysis of the band gap via absorption spectra because of intense light scattering in the pressurized ω phase. Contrary to earlier DFT predictions of metallicity,[34] our extinction and reflectance measurements show that ω-$NiMoO_4$ is a semiconductor with a direct band gap of 1.7 eV at ambient conditions. It must be noted that band gap energies were determined from the extinction spectra using Tauc plots[53] (inset of Figure 5). While this method is feasible for α-$NiMoO_4$, it is unsuitable for the pressure-transformed ω-$NiMoO_4$ due to multigrain formation at the $\alpha \rightarrow \omega$ phase transition. The intense light scattering reduces the transmitted intensity through the sample (I) below the detection limit of the spectrometer. We overcame this limitation by employing reflectance measurements (Figures 6 and S1), which allow band gap energy determination from the slight reflectivity jump associated with band gap absorption. This approach was validated by measuring the gap energy of α-$NiMoO_4$ for self-consistency. Although Tauc-plot analysis may introduce some uncertainty in the absolute band gap determination,[67] the excellent consistency between our experimental absorption, reflectance, and DFT results—all of which show mutual agreement within experimental and computational uncertainties—strongly supports the reliability of the observed trends and confirms the semiconducting nature of both phases (Figure 9).

Several key features of the metastable ω phase are evident: (i) its highest vibrational modes (852 and 762 cm^{-1}) are red-shifted relative to those of the α phase. This is due to the shorter Mo−O bond distances in α-$NiMoO_4$ involved in these vibrational modes (Figure 3, and Tables S1−S3); (ii) the ω-phase crystal-field splitting Δ = 0.92 eV is slightly smaller than in the α phase (Δ = 0.99 eV), a difference that persists under pressure (Figures 6 and 7). Although this reduction may seem counterintuitive for a denser polymorph, it arises from the shorter Ni−O bond lengths in the α phase (R_{Ni-O} = 2.034 Å

https://doi.org/10.1021/acs.chemmater.6c00849
Chem. Mater. XXXX, XXX, XXX−XXX

for Ni1, and 2.030 Å for Ni2), compared to the ω phase (R_{Ni-O} = 2.045 Å), together with greater distortion of the NiO_6 octahedra in the α phase (standard deviation σ_{Ni-O} = 0.05 Å, for both Ni sites) relative to the ω phase (σ_{Ni-O} = 0.02 Å). These electronic properties make ω-$NiMoO_4$ a promising candidate for photoactive applications.

CONCLUSIONS

We have demonstrated that α-$NiMoO_4$ remains stable under high pressure up to 14.5 GPa, beyond which it undergoes a structural transition to ω-$NiMoO_4$. This ω phase is metastable upon pressure release. DFT simulations predicted that the α and ω phases have similar enthalpies (difference of 34 meV), with 0 K $\alpha \rightarrow \omega$ transition pressure of ∼1 GPa accompanied by a volume collapse of −13%. This justifies the large hysteresis (∼13 GPa) leading to metastability at ambient conditions.

Raman modes were assigned to A_g and B_g symmetries within the monoclinic $C2/c$ space group for α-$NiMoO_4$ (monoclinic $P2/c$ for ω-$NiMoO_4$) based on strong agreement between experimental and DFT-calculated frequencies and pressure shifts. The Raman spectrum of the high-pressure phase serves as a reference for ω-$NiMoO_4$ ($P2/c$), complementing the α-phase single-crystal data.

Optical spectra and their pressure dependence confirmed that subgap bands originate from Ni^{2+} crystal-field transitions. At ambient conditions, the transitions from the $^3A_{2g}(F)$ ground state to the $^3T_{1g,a}(F)$ and $^1E_g(D)$ excited states show comparable intensities, a feature that we ascribe to Fano resonance. Pressure decouples these states, reducing the $^1E_g(D)$ intensity by an order of magnitude. Unlike $NiWO_4$, this indicates that exchange-mediated activation is weaker in α-$NiMoO_4$, with odd-parity electric-dipole activation mechanisms dominating.

The band gap of α-$NiMoO_4$ (2.99 eV) decreases with pressure, consistent with other molybdates containing open-shell transition-metal ions and confirmed by DFT simulations. The reduction accelerates above 5 GPa, reaching 2.28 eV at 14.5 GPa, where the transition to ω-$NiMoO_4$ occurs. This high-pressure phase exhibits electronic properties that correspond to a direct-gap semiconductor (E_{GAP} = 1.7 eV at ambient conditions), with Ni^{2+} subgap bands slightly shifted to lower energies (∼0.1 eV) compared to the α phase. These results indicate that ω-$NiMoO_4$ is better suited for photoactivity and remains metastable at ambient conditions after pressure release.

ASSOCIATED CONTENT

Data Availability Statement

The data that support the findings of this article are openly available at 10.5281/zenodo.19130704. Embargo periods may apply. The following files are available free of charge. Structure-1: DFT-calculated structures for α-, β'-, and ω-$NiMoO_4$. Raman-2: Raw Raman spectra at different pressures for α and ω phases. Optical Absorption and Reflectance-3: Raw optical extinction and reflectance spectra at different pressures for α and ω phases. Single-crystal X-ray diffraction data-4: Refined structural model for α-$NiMoO_4$ (CCDC Number: 2563519), structure factor file (FCF), and CIF validation report.

Supporting Information

The Supporting Information is available free of charge at https://pubs.acs.org/doi/10.1021/acs.chemmater.6c00849.

Crystallographic orientation of selected α-$NiMoO_4$ single crystals by X-ray diffraction and polarizing microscopy; variation of the lattice parameters of α-$NiMoO_4$ and β-$NiMoO_4$ with temperature; DFT-predictions for α-$NiMoO_4$, ω-$NiMoO_4$, and β'-$NiMoO_4$ phases; DFT-calculated phonon dispersion curves of $NiMoO_4$ for α and ω phases at several pressures; experimental and DFT-calculated Raman phonon frequencies and their pressure coefficients in α-$NiMoO_4$ and ω-$NiMoO_4$ at Γ-point; calculation of the crystal-field transition energies of Ni^{2+} in α-$NiMoO_4$ and their pressure dependence; p ressure dependence of the crystal transmittance of $NiMoO_4$ in the α and ω phases at 1550 nm (0.8 eV) (PDF)

Accession Codes

Deposition Number 2563510 contains the supplementary crystallographic data for this paper. These data can be obtained free of charge via the joint Cambridge Crystallographic Data Centre (CCDC) and Fachinformationszentrum Karlsruhe Access Structures service.

AUTHOR INFORMATION

Corresponding Author

Fernando Rodriguez − *MALTA Team, DCITIMAC, Facultad de Ciencias, Universidad de Cantabria, Santander 39005, Spain;* orcid.org/0000-0002-7237-7443; Email: rodriguf@unican.es

Authors

Luis Gómez − *Applied Physics Dept., Facultad de Ciencias, Universidad de Cantabria, Santander 39005, Spain*

Alfonso Muñoz − *Departamento de Física, MALTA Consolider Team, Universidad de La Laguna, San Cristóbal de La Laguna, Santa Cruz de Tenerife E-38200, Spain;* orcid.org/0000-0003-3347-6518

Helmut Ehrenberg − *Karlsruhe Institute of Technology (KIT), Institute for Applied Materials−Energy Storage Systems (IAM-ESS), Eggenstein-Leopoldshafen D-76344, Germany;* orcid.org/0000-0002-5134-7130

Complete contact information is available at: https://pubs.acs.org/10.1021/acs.chemmater.6c00849

Notes

Terms and Conditions: Most electronic Supporting Information files are available without a subscription to ACS Web Editions. Such files may be downloaded by article for research use (if there is a public use license linked to the relevant article, that license may permit other uses). Permission may be obtained from ACS for other uses through requests via the RightsLink permission system: http://pubs.acs.org/page/copyright/permissions.html.

The authors declare no competing financial interest.

ACKNOWLEDGMENTS

We thank Leire San Felices of the Servicio General de Rayos X (SGIker, UPV/EHU) for her assistance with the single-crystal diffraction measurements. Financial support from the Spanish State Research Agency (MCIN/AEI/10.13039/501100011033) is acknowledged through projects PID2022-138076NB-C44, PID2021-127656NB-I00, PID2025-

172909NB-C22 and the MALTA-Consolider Team (Grant No. RED2018-102612-T).

REFERENCES

(1) Sanyal, G.; Mondal, B.; Rout, C. S.; Chakraborty, B. Recent developments and future perspectives on energy storage and conversion applications of nickel molybdates. *Energy Storage* **2023**, *5* (6), No. e432.

(2) Ahn, J. H.; Park, G. D.; Kang, Y. C.; Lee, J. H. Phase-pure β-$NiMoO_4$ yolk-shell spheres for high-performance anode materials in lithium-ion batteries. *Electrochim. Acta* **2015**, *174*, 102.

(3) Lu, X.; Jia, W.; Chai, H.; Hu, J.; Wang, S.; Cao, Y. Solid-state chemical fabrication of one-dimensional mesoporous β-nickel molybdate nanorods as remarkable electrode material for supercapacitors. *J. Colloid Interface Sci.* **2019**, *534*, 322.

(4) Ratha, S.; Samantara, A. K.; Singha, K. K.; Gangan, A. S.; Chakraborty, B.; Jena, B. K.; Rout, C. S. Urea-assisted room temperature stabilized metastable β-$NiMoO_4$: experimental and theoretical insights into its unique bifunctional activity toward oxygen evolution and supercapacitor. *ACS Appl. Mater. Interfaces* **2017**, *9*, 9640.

(5) Gassoumi, B.; Jaballah, R.; Boukhachem, A.; Kamoun-Turki, N.; Amlouk, M. Simple route deposition and some physical investigations on nanoflower $NiMoO_4$ sprayed thin films. *Bull. Mater. Sci.* **2021**, *44* (2), 128.

(6) Yang, L.; Wang, J.; Wan, Y.; Li, Y.; Xie, H.; Cheng, H.; Seo, H. J. Structure and effective visible-light-driven photocatalytic activity of α-$NiMoO_4$ for degradation of methylene blue dye. *J. Alloys Compd.* **2016**, *664*, 756.

(7) Kong, Y.; Guo, Q.; Xiong, D.; Chai, N.; Jiang, Q.; Chen, T.; Yi, F. Y. Exploring P-(Fe, V)-Codoped Metastable-Phase β-$NiMoO_4$ for Improving the Performance of Overall Water Splitting. *Inorg. Chem.* **2025**, *64*, 1642.

(8) Ehrenberg, H.; Knapp, M.; Weitzel, H. *$\alpha \rightarrow \beta$-$NiMoO_4$ transition at high temperature HASYLAB Annual Report Part 1 Retrieved on February 2nd, 2026*; 2003. https://hasyweb.desy.de/science/annual_reports/2003_/index.html.

(9) Ehrenberg, H. *Structures, phase transitions, and properties of the 3d-transition metal oxomolybdate polymorphs $MeMoO_4$ Me= Mn, Fe, Co, Ni,Cu, and Zn; Habilitation thesis (Habilitationsschrift)*; Technical University of Darmstadt: Darmstadt, Germany, 2005.

(10) Wiesmann, M.; Ehrenberg, H.; Wltschek, G.; Zinn, P.; Weitzel, H.; Fuess, H. Crystal structures and magnetic properties of the high-pressure modifications of $CoMoO_4$ and $NiMoO_4$. *J. Magn. Magn. Mater.* **1995**, *150*, L1.

(11) Chen, M.; Wu, J. L.; Liu, Y. M.; Cao, Y.; Guo, L.; He, H. Y.; Fan, K. N. A practical grinding-assisted dry synthesis of nanocrystalline $NiMoO_4$ polymorphs for oxidative dehydrogenation of propane. *J. Solid State Chem.* **2011**, *184*, 3357.

(12) Ehrenberg, H.; Svoboda, I.; Wltschek, G.; Wiesmann, M.; Trouw, F.; Weitzel, H.; Fuess, H. Crystal and magnetic structure of α-$NiMoO_4$. *J. Magn. Magn. Mater.* **1995**, *150*, 371.

(13) Syassen, K. Ruby under pressure. *High Pressure Res.* **2008**, *28*, 75.

(14) Klotz, S.; Chervin, J.; Munsch, P.; Le Marchand, G. Hydrostatic limits of 11 pressure transmitting media. *J. Phys. D: Appl. Phys.* **2009**, *42*, 075413.

(15) Martín-Sánchez, C.; Barreda-Argüeso, J. A.; Seibt, S.; Mulvaney, P.; Rodríguez, F. Effects of hydrostatic pressure on the surface plasmon resonance of gold nanocrystals. *ACS Nano* **2019**, *13*, 498−504.

(16) Barreda-Argüeso, J. A.; Rodríguez, F. *Microscopio para la caracterización espectroscópica de una muestra*; Universidad de Cantabria, 2013.

(17) Hohenberg, P.; Kohn, W. Inhomogeneous Electron Gas. *Phys. Rev.* **1964**, *136*, B864−871.

(18) Kresse, G.; Furthmüller, J. Efficiency of ab-initio total energy calculations for metals and semiconductors using a plane-wave basis set. *Comput. Mater. Sci.* **1996**, *6*, 15−50.

(19) Kresse, G.; Furthmüller, J. Efficient iterative schemes for ab initio total-energy calculations using a plane-wave basis set. *Phys. Rev. B* **1996**, *54*, 11169.

(20) Blöchl, P. E. Projector augmented-wave method. *Phys. Rev. B* **1994**, *50*, 17953.

(21) Kresse, G.; Joubert, D. From ultrasoft pseudopotentials to the projector augmented-wave method. *Phys. Rev. B* **1999**, *59*, 1758.

(22) Perdew, J. P.; Ruzsinszky, A.; Csonka, G. I.; Vydrov, O. A.; Scuseria, G. E.; Constantin, L. A.; Zhou, X.; Burke, K. Restoring the density-gradient expansion for exchange in solids and surfaces. *Phys. Rev. Lett.* **2008**, *100*, 136406.

(23) Dudarev, S. L.; Botton, G. A.; Savrasov, S. Y.; Humphreys, C.; Sutton, A. P. Electron-energy-loss spectra and the structural stability of nickel oxide: An LSDA+ U study. *Phys. Rev. B* **1998**, *57*, 1505.

(24) Sanchez-Martin, J.; Pellicer-Porres, J.; Liang, A.; Ibanez, J.; Oliva, R.; Popescu, C.; He, Z.; Rodriguez-Hernandez, P.; Muñoz, A.; Errandonea, D. High-Pressure Vibrational and Structural Properties of $Ni_3V_2O_8$ and $Co_3V_2O_8$ up to 20 GPa. *J. Phys. Chem. C* **2023**, *127*, 21684−21694.

(25) Birch, F. Finite elastic strain of cubic crystals. *Phys. Rev.* **1947**, *71*, 809.

(26) Togo, A. First-principles phonon calculations with phonopy and phono3py. *J. Phys. Soc. Jpn.* **2023**, *92*, 012001.

(27) Wang, V.; Xu, N.; Liu, J.-C.; Tang, G.; Geng, W.-T. VASPKIT: A user-friendly interface facilitating high-throughput computing and analysis using VASP code. *Comput. Phys. Commun.* **2021**, *267*, 108033.

(28) Perdew, J. P.; Levy, M. Physical content of the exact Kohn-Sham orbital energies: band gaps and derivative discontinuities. *Phys. Rev. Lett.* **1983**, *51*, 1884.

(29) Sham, L. J.; Schlüter, M. Density-functional theory of the energy gap. *Phys. Rev. Lett.* **1983**, *51*, 1888.

(30) Ouahrani, T.; Boufatah, R. M.; Benaissa, M.; Morales-García, Á.; Badawi, M.; Errandonea, D. Effect of intrinsic point defects on the catalytic and electronic properties of Cu_2 WS_4 single layer: Ab initio calculations. *Phys. Rev. Mater.* **2023**, *7*, 025403.

(31) Sleight, A. W.; Chamberland, B. L. Transition metal molybdates of the type $AMoO_4$. *Inorg. Chem.* **1968**, *7*, 1672.

(32) Chaturvedi, S.; Rodriguez, J. A.; Brito, J. L. Characterization of pure and sulfided $NiMoO_4$ catalysts using synchrotron-based X-ray absorption spectroscopy (XAS) and temperature-programmed reduction (TPR). *Catal. Lett.* **1998**, *51*, 85.

(33) Young, A. P.; Schwartz, M. C. High-pressure synthesis of molybdates with the wolframite structure. *Science* **1963**, *141*, 348.

(34) Matar, S. F.; Largeteau, A.; Demazeau, G. $AMoO_4$ (A= Mg, Ni) molybdates: Phase stabilities, electronic structures and chemical bonding properties from first principles. *Solid State Sci* **2010**, *12*, 1779.

(35) Sieber, K.; Kershaw, R.; Dwight, K.; Wold, A. Dependence of magnetic properties on structure in the systems nickel (II) molybdate (VI) and cobalt (II) molybdate (VI). *Inorg. Chem.* **1983**, *22*, 2667.

(36) Heiba, B.; Chinarro, E.; Colomer, M. T.; Jurado, J. R. Combustion synthesis and electrical behavior of nanometric β-$NiMoO_4$. *J. Phys. Chem. C* **2010**, *114* (10), 4251.

(37) de Moura, A. P.; de Oliveira, L. H.; Rosa, I. L.; Xavier, C. S.; Lisboa-Filho, P. N.; Li, M. S.; Porta, F. A. L.; Longo, E.; Varela, J. A. Structural, optical, and magnetic properties of $NiMoO_4$ nanorods prepared by microwave sintering. *Sci. World J.* **2015**, *2015* (1), 315084.

(38) Heiba, Z. K.; Abdellatief, M.; Mohamed, M. B.; Badawi, A. Investigating the electronic structure and UV−Vis−NIR optical properties of α-$NiMoO_4$ nanoparticles. *J. Mater. Sci.: Mater. Electron.* **2025**, *36*, 330.

(39) Harshan, H.; Priyanka, K. P.; Sreedevi, A.; Jose, A.; Varghese, T. Structural, optical and magnetic properties of nanophase $NiWO_4$ for potential applications. *Eur. Phys. J. B* **2018**, *91* (11), 287.

(40) Uitert, L. G. V.; Sherwood, R. C.; Williams, H. J.; Rubin, J. J.; Bonner, W. A. Magnetic properties of a number of divalent transition metal tungstates, molybdates and titanates. *J. Phys. Chem. Solids* **1964**, *25* (12), 1447.

(41) Ehrenberg, H.; Wiesmann, M.; Paulus, H.; Weitzel, H. Magnetic phase diagrams of α-$NiMoO_4$. *J. Magn. Magn. Mater.* **1998**, *186*, 74.
(42) Liu, C. B.; He, Z. Z.; Liu, Y. J.; Chen, R.; Shi, M. M.; Zhu, H. P.; Wang, J. F.; Wang, J. F. Magnetic anisotropy and spin-flop transition of $NiWO_4$ single crystals. *J. Magn. Magn. Mater.* **2017**, *444*, 190.
(43) Kuzmin, A.; Kalinko, A.; Evarestov, R. A. First-principles LCAO study of phonons in $NiWO_4$. *Cent. Eur. J. Phys.* **2011**, *9*, 502−509.
(44) Martín-Sánchez, C.; Sánchez-Iglesias, A.; Barreda-Argüeso, J. A.; Polian, A.; Itié, J. P.; Pérez, J.; Mulvaney, P.; Liz-Marzán, L. M.; Rodríguez, F. On the Stiffness of Gold at the Nanoscale. *ACS Nano* **2021**, *15*, 19128.
(45) Errandonea, D.; Rodriguez, F.; Vilaplana, R.; Vie, D.; Garg, S.; Nayak, B.; Garg, N.; Singh, J.; Kanchana, V.; Vaitheeswaran, G. Band-gap energy and electronic d−d transitions of $NiWO_4$ studied under high-pressure conditions. *J. Phys. Chem. C* **2023**, *127*, 15630.
(46) Abdel-Dayem, H. M. Dynamic phenomena during reduction of α-$NiMoO_4$ in different atmospheres: in-situ thermo-Raman spectroscopy study. *Ind. Eng. Chem. Res.* **2007**, *46*, 2466.
(47) Popovych, O. M.; Budzulyak, I. M.; Yuhymchuk, V. O.; Budzulyak, S. I.; Popovych, D. I. Raman spectroscopy of nickel molybdate and its modifications. *Fullerenes, Nanotubes Carbon Nanostruct.* **2021**, *29* (12), 1009.
(48) Coelho, M. N.; Freire, P. T. C.; Maczka, M.; Luz-Lima, C.; Saraiva, G. D.; Paraguassu, W.; Filho, A. G. S.; Pizani, P. S. High-pressure Raman scattering of $MgMoO_4$. *Vib. Spectrosc.* **2013**, *68*, 34−39.
(49) Gao, X.; Zheng, Z.; Xiong, M.; Qian, L.; Yan, H. Structural Evolution of $CoMoO_4$ under Pressure: Multiphase Transformations and Reconstructive Behaviors. *Inorg. Chem.* **2026**, *65*, 234.
(50) Ruiz-Fuertes, J.; López-Moreno, S.; Errandonea, D.; Pellicer-Porres, J.; Lacomba-Perales, R.; Segura, A.; Rodríguez-Hernández, P.; Muñoz, A.; Romero, A. H.; González, J. High-pressure phase transitions and compressibility of wolframite-type tungstates. *J. Appl. Phys.* **2010**, *107* (8), 083506.
(51) Garg, S.; Verma, A. K.; Poswal, H. K.; Nicacio, T. C. N.; Errandonea, D.; Garg, N. High pressure investigation of structural and electronic behavior of β-$ZnMoO_4$. *J. Alloys Compd.* **2025**, *1010*, 177515.
(52) Meullemeestre, J.; Penigault, E. Les molybdates neutres de magnesium. *Bull. Soc. Chim. Fr* **1975**, *9−10*, 1925−1932.
(53) Tauc, J. Optical properties and electronic structure of amorphous Ge and Si. *Mater. Res. Bull* **1968**, *3*, 37.
(54) Sugano, S.; Tanabe, Y.; Kamimura, H. *Multiplets of Transition-Metal Ions in Crystals*; Academic Press: New York, 1970.
(55) Griffith, J. S. *The Theory of Transition-Metal Ions*; Cambridge University Press: Cambridge, 1964.
(56) Hernández, I.; Rodríguez, F.; Tressaud, A. Optical properties of the $(CrF_6)^3$ complex in A_2 BMF_6: Cr^{3+} elpasolite crystals: variation with M-F bond distance and hydrostatic pressure. *Inorg. Chem.* **2008**, *47*, 10288.
(57) Zhang, Y.; Holzwarth, N. A. W.; Williams, R. T. Electronic band structures of the scheelite materials $CaMoO_4$, $CaWO_4$, $PbMoO_4$, and $PbWO_4$. *Phys. Rev. B* **1998**, *57*, 12738.
(58) Burns, R. G. *Mineralogical Applications of Crystal Field Theory*, 2nd ed.; Cambridge University Press: Cambridge, 1993.
(59) Ferguson, J.; Guggenheim, H. J. Electronic Absorption Spectrum of Ni (II) in Cubic Perovskite Fluorides. II. Concentration and Exchange Effects. *J. Chem. Phys.* **1966**, *44*, 1095.
(60) Pappalardo, R.; Wood, D. L.; Linares, R. C., Jr Optical absorption spectra of Ni-doped oxide systems. I. *J. Chem. Phys.* **1961**, *35*, 1460.
(61) Koetke, J.; Petermann, K.; Huber, G. Infrared excited state absorption of Ni^{2+} doped crystals. *J. Lumin.* **1994**, *60−61*, 197−200.
(62) Pérez-Francés, D.; Rodríguez, F.; Valiente, R. Optical spectroscopy of exchange-coupled ions: Insights into homonuclear, heteronuclear and mixed transition-metal/rare-earth systems. *Opt. Mater.* **2025**, *163*, 116965.
(63) Barreda-Argüeso, J. A.; Rodríguez, F. Pressure dependence of the crystal-field spectrum of $KNiF_3$: Single and double excitations. *Phys. Rev. B* **2021**, *103*, 085115.
(64) Newman, R.; Chrenko, R. M. Optical properties of nickel oxide. *Phys. Rev.* **1959**, *114*, 1507.
(65) Fano, U. Effects of configuration interaction on intensities and phase shifts. *Phys. Rev.* **1961**, *124*, 1866.
(66) Ruiz-Fuertes, J.; López-Moreno, S.; López-Solano, J.; Errandonea, D.; Segura, A.; Lacomba-Perales, R.; Muñoz, A.; Radescu, S.; Rodríguez-Hernández, P.; Gospodinov, M.; Nagornaya, L. L.; Tu, C. Y. Pressure Effects on the Electronic and Optical Properties of AWO_4 Wolframites (A = Cd, Mg, Mn, and Zn): The Distinctive Behavior of Multiferroic $MnWO_4$. *Phys. Rev. B* **2012**, *86*, 125202.
(67) Garg, A. B.; Vie, D.; Rodriguez-Hernandez, P.; Muñoz, A.; Segura, A.; Errandonea, D. Accurate determination of the bandgap energy of the rare-earth niobate series. *J. Phys. Chem. Lett.* **2023**, *14*, 1762−1768.